

Article

A Numerical Simulation of Convective Systems in Southeast China: A Comparison of Microphysical Schemes and Sensitivity Experiments on Raindrop Break and Evaporation

Zhaoqing Cheng^{1,2} and Xiaoli Liu^{1,2,*} 

¹ China Meteorological Administration Aerosol-Cloud and Precipitation Key Laboratory, Nanjing University of Information Science and Technology, Nanjing 210044, China; 202212480011@nuist.edu.cn

² College of Atmospheric Physics, Nanjing University of Information Science and Technology, Nanjing 210044, China

* Correspondence: liuxiaoli2004y@nuist.edu.cn

Abstract: This study employed version 4.2.2 of the Weather Research and Forecasting (WRF) model for this simulation and applied two microphysics schemes, the Thompson scheme (THOM) and Milbrandt–Yau scheme (MY)—which are widely used in convective simulations—to simulate a mesoscale severe convective precipitation event that occurred in southeastern China on 8 May 2017. The simulations were then compared with dual-polarization radar observations using a radar simulator. It was found that THOM produced vertical structures of radar reflectivity (Z_H) closer to radar observations and accumulated precipitation more consistent with ground-based observations. However, both schemes overestimated specific differential phase (K_{DP}) and differential reflectivity (Z_{DR}) below the 0 °C level. Further analysis indicated that THOM produced more rain with larger raindrop sizes below the 0 °C level. Due to the close connection between raindrop breakup, evaporation rate, and raindrop size, sensitivity experiments on the breakup threshold (D_b) and the evaporation efficiency (E_E) of the THOM scheme were carried out. It was found that adjusting D_b significantly changed the simulated raindrop size distribution and had a certain impact on the strength of cold pool; whereas modifying E_E not only significantly changed the intensity and scope of the cold pool, but also had great effect on the raindrop size distribution. At the same time, comparison with dual-polarization radar observations indicated that reducing the D_b can improve the model's simulation of polarimetric radar variables such as Z_{DR} . This paper specifically analyzes a severe convective precipitation event in the Guangdong region under weak synoptic conditions and a humid climate. It demonstrates the feasibility of a method based on polarimetric radar data that modifies D_b of THOM to achieve better consistency between simulations and observations in southeast China. Since the microphysical processes of different Mesoscale Convective Systems (MCSs) vary, the generalizability of this study needs to be validated through more cases and regions in the future.

Keywords: cloud microphysics parameterization; dual-polarization radar simulator; raindrop breakup; evaporation of raindrop



Citation: Cheng, Z.; Liu, X. A Numerical Simulation of Convective Systems in Southeast China: A Comparison of Microphysical Schemes and Sensitivity Experiments on Raindrop Break and Evaporation. *Remote Sens.* **2024**, *16*, 4297. <https://doi.org/10.3390/rs16224297>

Academic Editor: Yaoming Ma

Received: 13 August 2024

Revised: 7 November 2024

Accepted: 14 November 2024

Published: 18 November 2024



Copyright: © 2024 by the authors. Licensee MDPI, Basel, Switzerland. This article is an open access article distributed under the terms and conditions of the Creative Commons Attribution (CC BY) license (<https://creativecommons.org/licenses/by/4.0/>).

1. Introduction

The Guangdong province is located in southeastern China and it has a complex terrain. It is also one of the regions with the highest rainfall in the world, with annual precipitation exceeding 2000 mm [1]. Approximately 40–50% of the yearly rainfall occurs during the pre-summer rainy season (PSRS) from April to June [1]. Extreme precipitation events cause severe disasters every year, posing serious threats to life safety and social stability [2,3]. Therefore, high-precision and high-resolution assessments of the timing and intensity of precipitation has become an urgent issue that needs to be addressed [4–6].

Currently, Numerical Weather Prediction (NWP) models remain the primary tool for forecasting convective weather. However, due to the inadequate understanding of cloud microphysical processes [7,8] and the imprecision in the parameterization of the microphysical schemes [9–11], there is still significant uncertainty in the microphysical schemes within the models when simulating cloud microphysical processes [12]. This uncertainty leads to poor performance of numerical models in simulating the accumulated precipitation amount and the location of heavy rainfall in urban areas [13,14].

During the development of convection, a relatively colder and denser air mass may form at the base of the convective system, which is referred to as a cold pool [15]. The intensity of the cold pool can influence the organization, dynamic structure, and thermodynamic structure of the ascending/descending airflows associated with convective systems, thereby affecting the formation and development of convection [9,16,17].

As the cold pool forms and expands, the cold air replaces the warmer air, causing the warm air to be lifted, which in turn leads to the formation of new clouds [18]. Furthermore, the downdrafts associated with the cold pool enhance the sensible and latent heat fluxes, thereby altering the thermodynamic properties and moisture structure below the clouds [19]. Convective cold pools play a significant role in various aspects of MCSs, including the maintenance of squall lines and the transition of tropical convection from weak to strong stages [20,21]. Additionally, it has also been shown that the self-sustaining mechanisms of cold pools can lead to the prolonged maintenance of rainbands, resulting in the persistence of heavy rainfall [22]. In the process of convective precipitation, raindrops undergo various microphysical processes such as coalescence, breakup, and evaporation as they fall from the cloud to the ground. Among these, the breakup of raindrops directly affects the raindrop size distribution, which in turn affects the evaporation rate, thus affecting the evolution of the cold pool [23–25]. The intense latent heat fluxes are brought by the evaporation of rainwater, playing a significant role in the formation of cold pools [19].

Studies have demonstrated that microphysical processes are crucial for accurately forecasting heavy rainfall in southeastern China. Qian et al. [17] pointed out that a lower rain evaporation rate and the resulting weaker cold pool were the reasons for the failure of simulating the convective system in southeastern China. By use of three microphysical schemes, Zhou et al. [26] pointed out that all simulations produced weaker cold pools compared to the observations, and improving the simulated cold pool intensity and drop size distributions (DSDs) led to a significant improvement in surface precipitation. Lompar et al. [27] incorporated the first gust front pulsation parameterization scheme into the WRF, which not only improved the intensity and distribution of the cold pool but also enhanced the overall simulation performance.

With the development of dual-polarization radar detection technology, polarimetric radar observations have become widely used to compare the microphysical characteristics of heavy rainfall between observations and the NWP models [28,29]. Polarimetric radar is capable of transmitting and receiving polarized electromagnetic waves in two orthogonal directions. Because the polarization of the echo is influenced by particle properties, it can provide rich microphysical characteristic information such as the phase state, density, and shape of hydrometeors [30,31]. In addition to the radar reflectivity (Z_H) for horizontal polarization, there are two other commonly used polarimetric variables. One is the differential reflectivity (Z_{DR}), which reflects the shape and size of hydrometeors, and the other is the specific differential phase (K_{DP}), which primarily indicates the liquid water content within the sampling volume [31–33]. The combination of Z_H and Z_{DR} can reveal the characteristics of drop size distributions (DSDs) as well as the “fingerprints” of microphysical processes such as evaporation, coalescence, and breakup [32,34]. This paper will compare simulation results from NWP models with polarimetric radar observations by converting model output data into polarimetric radar data by the use of a radar simulator [35,36].

Meteorologists typically use NWP models with complex physical parameterization schemes to simulate and understand the mechanisms of weather systems [37]. Compared to bin microphysics schemes, bulk microphysics schemes offer superior computational effi-

ciency, and are extensively utilized in both scientific research and operational contexts [10]. Two-moment (2M) bulk microphysical schemes generally forecast two parameters—the intercept parameter N_0 and the slope parameter λ —while one moment (1M) bulk schemes prespecify N_0 [7,38]. Due to the increased flexibility in parameter prediction, 2M schemes often produce better simulation results when evaluated against observational data than 1M schemes [8,11,39]. Therefore, this study employs two microphysics 2M schemes, the Thompson scheme (THOM) and Milbrandt–Yau scheme (MY), which are widely used in convective simulations.

The focus of this study is comparing polarimetric radar data with simulation results, evaluating and improving the parameterization scheme’s representation of macroscopic and microscopic features of the convective system. The structure of this paper is as follows: Section 2 introduces the radar data, simulation settings, and the radar simulator used in this study. Section 3 compares and analyzes the composite radar reflectivity, vertical cross-sections of radar polarimetric variables, and 18-hour accumulated precipitation from observations and simulations, and continues to compare and analyze different aspects of the simulation, including the hydrometeor mixing ratios, hydrometeor source and sink terms, cold pool, and the raindrop mass-weighted diameter ($D_{m,r}$) distribution. Section 4 modifies the parameters related to raindrop breakup and evaporation and assesses the results of these modifications. Finally, Section 5 discusses the results, and Section 6 draws conclusions and proposes possible measures for further improvement.

2. Materials and Methods

2.1. Radar Data

The radar data are derived from the Guangzhou S-band dual-polarization radar (Z9200; 23.00°N, 113.36°E), which was put into operation in May 2016. The radar operates in a dual-transmit dual-receive mode with a wavelength of 10 cm, an azimuthal resolution of 1°, a radial resolution of 250 m, and an observation radius of 230 km. This radar can provide a series of dual-polarization variables, including reflectivity (Z_H), differential reflectivity factor (Z_{DR}), correlation coefficient (CC), specific differential phase (K_{DP}), and differential phase (φ_{DP}), which can characterize the microphysical structure of precipitation. The volume scan time of the dual-polarization radar is approximately 6 min, using the VCP21D scanning pattern, which includes nine elevation angles: 0.5°, 1.5°, 2.4°, 3.3°, 4.3°, 6.0°, 9.9°, 14.6°, and 19.5°.

2.2. Simulation Settings

On 8 May 2017, a significant convective precipitation event occurred in Guangdong, China, and the local development was rapid, with extreme precipitation intensity. On a spatial scale, the mature squall line was approximately 800 km long and 40 km wide, advancing at a speed of 30 to 40 km per h, sweeping across much of the Guangdong province [40]. In this study, we simulated the case using the generation mesoscale numerical model WRF and employed version 4.2.2 of the WRF-ARW. For the simulation, the THOM and MY microphysics schemes within the WRF model were selected. The simulation used two-layer nested domains with resolutions of 3 km for the outer and 1 km for the inner domain. The simulation period spanned from 18:00 UTC on 7 May 2017 to 18:00 UTC on 8 May 2017. The spin-up time of the model was set to 6 h, and the numerical simulation results following 00:00 UTC on 8 May 2017 were compared with radar observations. The initial and boundary field data were obtained from ERA5 with a resolution of $0.25^\circ \times 0.25^\circ$. The boundary layer scheme chosen was the Mellor–Yamada–Janjic (Eta) TKE scheme, and the surface layer scheme used was the Monin–Obukhov (Janjic Eta) scheme. The land-surface process scheme employed was the unified Noah land-surface model with the Rapid Radiative Transfer Model (RRTM) for the Global Climate Model (GCM) for shortwave and longwave radiation. The cumulus parameterization was turned off in two domains. This convective process occurred in Qingyuan City, Guangdong province. Therefore, two nested domains, d01 and d02, were set up, centered on Qingyuan City, with

both domains consisting of 481×481 grid points. The setup of the simulation domain is shown in Figure 1.

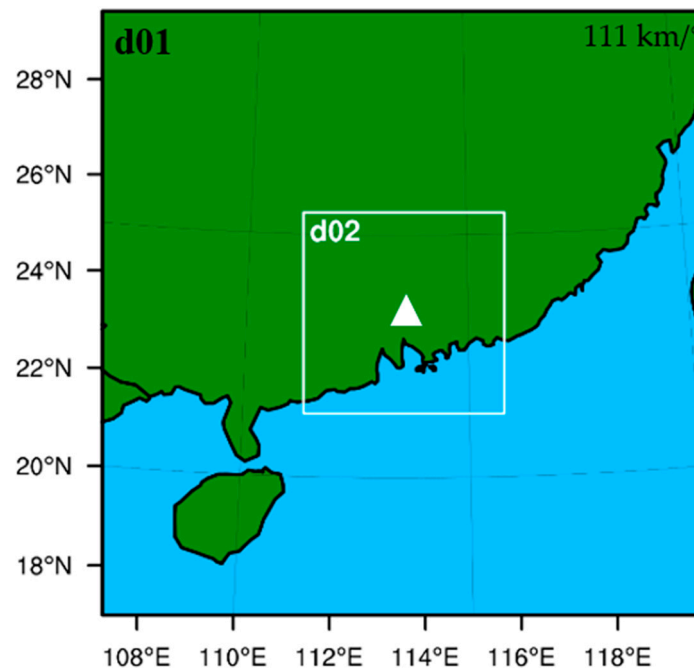


Figure 1. The numerical simulation domain setup. The numerical simulation involved two-way nested domains, d01 and d02. The white triangle marks the location of Qingyuan City.

This study delves into two extensively utilized 2M cloud microphysics schemes: THOM [41] and MY [42]. As shown in Table 1, THOM predicts the mixing ratios (q) for cloud water, rain, cloud ice, snow, and graupel, as well as the number concentrations (N) specifically for rain and cloud ice. Conversely, MY forecasts q and N for a broader spectrum of hydrometeors, including cloud water, rain, cloud ice, snow, graupel, and hail.

Table 1. Summary of microphysics options for THOM and MY schemes.

Scheme	Mass Ratio	Number Concentration
THOM	q_c, q_r, q_i, q_s, q_g	N_r, N_i
MY	$q_c, q_r, q_i, q_s, q_g, q_h$	$N_c, N_r, N_i, N_s, N_g, N_h$

c: cloud; *r*: rain; *i*: ice; *s*: snow; *g*: graupel; *h*: hail.

2.3. Radar Simulator

This paper utilizes the Polarimetric Radar Simulator (CAPS-PRS) developed by the Center for Analysis and Prediction of Storms (CAPS) at the University of Oklahoma, USA for non-hydrostatic weather forecasting models with explicit microphysics schemes. It includes calculations of reflectivity for horizontal and vertical polarizations, K_{DP} , Z_{DR} , ρ_{hv} . This simulator is capable of simulating polarimetric radar measurements in the weather radar frequency band and can take forecast variables simulated by NWP models using single-moment, two-moment, and three-moment microphysics schemes as inputs [43].

3. Results Analysis

3.1. Comparison Analysis of Observational and Simulated Results

3.1.1. Assessment of Convective System Simulations

The intense convective precipitation process in the Guangdong region was divided into three stages: development, maturity, and dissipation. The radar observations of composite reflectivity clearly illustrate the evolution of the MCS (Figure 2(a1–c1)). The

convective cloud began to form outside of the Guangdong region, and then rapidly developed into a convective band by 0600 UTC, moving southeastward and continuing to develop (Figure 2(a1)). During the development stage (0600 UTC), both the convective and stratiform cloud areas expanded rapidly. By the time the system reached its maturity stage (0854 UTC), the front was characterized by a high and strong convective band associated with heavy rainfall, marking the peak of convective activity (the time with the highest hourly precipitation amount) (Figure 2(b1)). Other notable features included a transition zone with lower radar reflectivity directly following the convective zone. As the system entered the dissipation phase (1200 UTC), the convective cloud band began to weaken, and mesoscale organization gradually diminished (Figure 2(c1)).

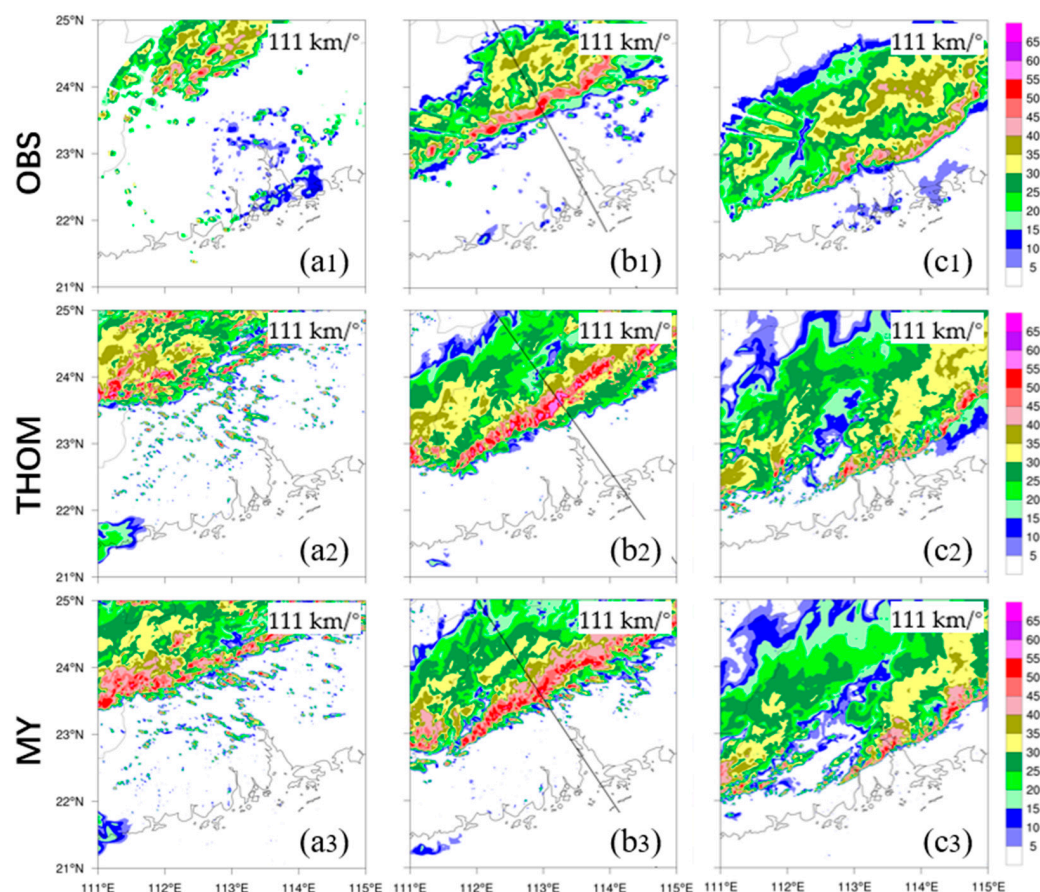


Figure 2. The composite reflectivity (units: dBZ) from radar observations (a1–c1) at 0600, 0854, and 1200 UTC; the composite reflectivity from the THOM simulation (a2–c2) at 0630, 0930, and 1230 UTC and the MY simulation (a3–c3) at 0630, 0830, and 1200 UTC. The black lines represent the vertical cross-section transects.

Overall, by comparing the simulated composite reflectivity with the observation, both schemes simulate the development trends, intensities, and spatial positions of the convective process at different stages well. The three stages to the simulations by THOM correspond to 0630 UTC (Figure 2(a2)), 0930 UTC (Figure 2(b2)), and 1230 UTC (Figure 2(c2)), as well as to the simulations by MY at 0630 UTC (Figure 2(a3)), 0830 UTC (Figure 2(b3)), and 1200 UTC (Figure 2(c3)). The convective development simulated by THOM is slower compared to the observations, causing a delay in the timing of the mature and dissipation stages. In contrast, MY simulated faster convective development, resulting in an earlier timing for the mature stage. The reflectivity intensity in the convective region is stronger than the observed values, and the reflectivity intensity simulated by the MY scheme is weaker than that of the THOM scheme.

3.1.2. Analysis of Radar Polarimetric Parameters

Due to the similar vertical structures of observed and simulated characteristics in three stages of this MCS, this section will only focus on the mature stage. Figure 3 presents the vertical cross-sections of radar polarimetric parameters during the mature stage, with the transects indicated by the black lines shown in Figure 2. These transects are nearly perpendicular to the convective system, and their positions were selected to simultaneously observe the vertical structural characteristics of the convective region, stratiform region, and transition zone during the mature stage.

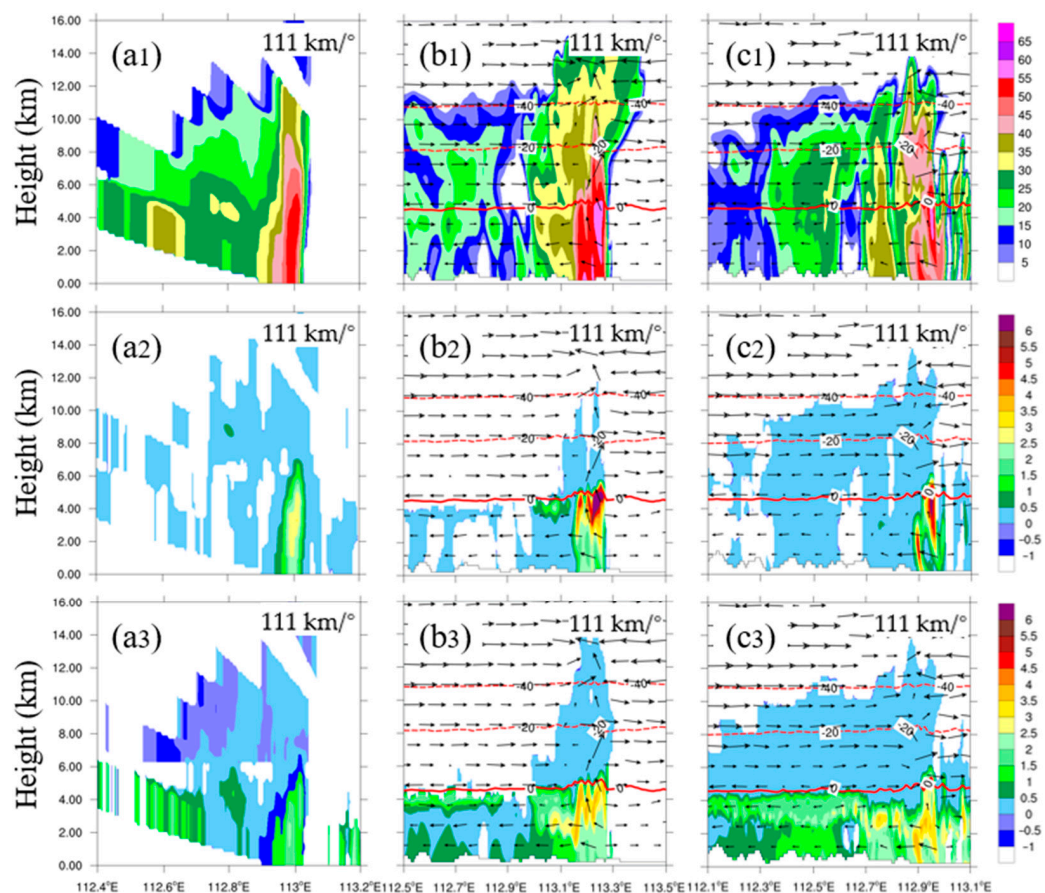


Figure 3. Vertical cross-sections of polarimetric parameters during the mature stage of convections from radar observations and model simulations; (a1–a3, b1–b3, c1–c3) represent the Z_H (units: dBZ), K_{DP} (units: $^{\circ}/\text{km}$), and Z_{DR} (units: dB) from the radar observations of THOM, and MY, respectively. The red dashed and solid lines in the figures are the isotherms of -40°C , -20°C , and 0°C , where the black arrows indicate the wind field.

As the convective system enters the mature stage (Figure 3(a1)), the radar echo coverage expands significantly, the echo tops surpass 16 km in altitude, while the strong echo zones ($Z_H > 40$ dBZ) ascend to around 9 km (Figure 3(a1)). THOM simulates radar echo tops reaching above 15 km, with the strong echo zones rising to around 10 km. Below the 0°C layer, the THOM-simulated Z_H slightly exceeds the observed values, with peak values exceeding 55 dBZ (Figure 3(b1)). In contrast, the MY scheme produces echo tops approximately at 14 km, with the strong echo zones ascending close to the -40°C isotherm. Below the 0°C layer, Z_H reaches above 50 dBZ, and notably, there remains a vast area of strong echoes in the upper cloud area (Figure 3(c1)). Both THOM and MY generate extensive stratiform cloud regions and successfully simulate the transition zone. However, Z_H in the stratiform areas generated by both schemes is lower than that which is observed by radar.

In the vertical cross-sections of the radar observations for Z_H and Z_{DR} (Figure 3(a1,a3)), the stratiform cloud region behind is separated from the forward convective region by a

weak echo transition zone with lower Z_H and Z_{DR} values. The Z_{DR} in the stratiform and convective regions shows a significant increase with decreasing altitude below the 0°C level, with the Z_{DR} maxima ($\sim 1.5\text{--}2.5$ dB) existing below the 4 km altitude (Figure 3(a3)). In the convective region, K_{DP} values exceeding $0.5^\circ/\text{km}$ are observed in the upper part of the columnar Z_{DR} , which may be due to the presence of supercooled raindrops adjacent to the updraft or hail coated with supercooled water [44,45]. The increase in K_{DP} below the 0°C level in the convective region is associated with high Z_H (>45 dBZ). This may be related to ice particles melting too quickly below the 0°C level, which need to be further analyzed.

It is noted that K_{DP} primarily represents the content of liquid water per unit volume [26]. Although the structures of the observed and the simulated K_{DP} are similar, both schemes overestimated the K_{DP} values below the 0°C layer in the convective region (Figure 3(a2–c2)). This situation is different from the simulations under North American climatic conditions, where both microphysical schemes produced weaker K_{DP} values than observed [46].

Like K_{DP} , both schemes simulate higher Z_{DR} values below the 0°C layer than what is observed (Figure 3(a3–b3)). Larger Z_{DR} values indicate a greater difference in the horizontal and vertical dimensions of the particles, which is a significant microphysical factor for pure and large size rain [31]. This suggests that, in comparison to radar observations, the raindrop size within the convective area below the 0°C layer is overestimated by both schemes.

It is shown that the MY's microphysical scheme simulates stronger radar reflectivity zones compared to the observations, whereas the THOM's simulated radar reflectivity is more closely aligned with the observations. Both schemes simulate a weak echo transition zone between the convective and stratiform regions, corresponding to the radar observations, with the Z_{DR} and K_{DP} simulated by both schemes being significantly greater than the observation below the 0°C level in the convective region.

3.1.3. Comparison of the Accumulated Precipitation

Figure 4 shows the accumulated surface precipitation from the onset to the dissipation of the convective system (from 0000 to 1800 UTC, 8 May 2017). Generally, both schemes basically reproduced the distribution of surface precipitation, albeit with narrower precipitation areas compared to the ground observations. Both schemes simulated more heavy precipitation centers than observed with greater intensity and underpredicted intensity of precipitation in the southwest of the Guangzhou radar (Figure 4a–c). Considering the distribution and magnitude of several precipitation centers observed, THOM exhibited more concentrated and widespread precipitation centers in the areas north of the Guangzhou radar, leading to a better representation of precipitation (Figure 4b). The MY scheme simulated a similar precipitation pattern with respect to the THOM scheme, but with more scattered precipitation centers north of the Guangzhou radar (Figure 4c). This suggests that the inherent differences in microphysical schemes could significantly impact the precipitation patterns and rainfall rates.

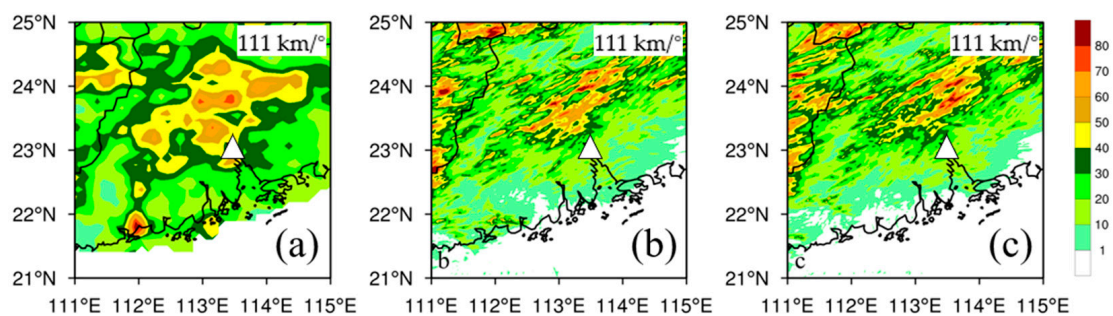


Figure 4. The 18-h accumulated precipitation (units: mm) from 0000 to 1800 UTC on 8 May 2017, obtained from ground observation stations (a), THOM (b), and MY (c). The white triangle marks the location of the radar (GZRD).

3.2. Analysis of the Simulation Results

3.2.1. Vertical Distribution of Hydrometeors

Figure 5 presents the vertical profiles of the regional averaged hydrometeors mixing ratio (q) during the mature stages of the convective event. There is a significant difference in snow mixing ratio for the two schemes, which may relate to the different microphysical treatments of snow. Previous studies have noted that THOM has a broader distribution of snow due to its special treatment of snow [9,16,47], which helps THOM to better simulate convective and stratiform cloud regions [46,48,49]. It is noteworthy that the two schemes, which differ significantly in the treatment of ice-phase particles, produce similar surface precipitation (Figure 4) as well as mixing ratios of rain (Figure 5), which must be further analyzed.

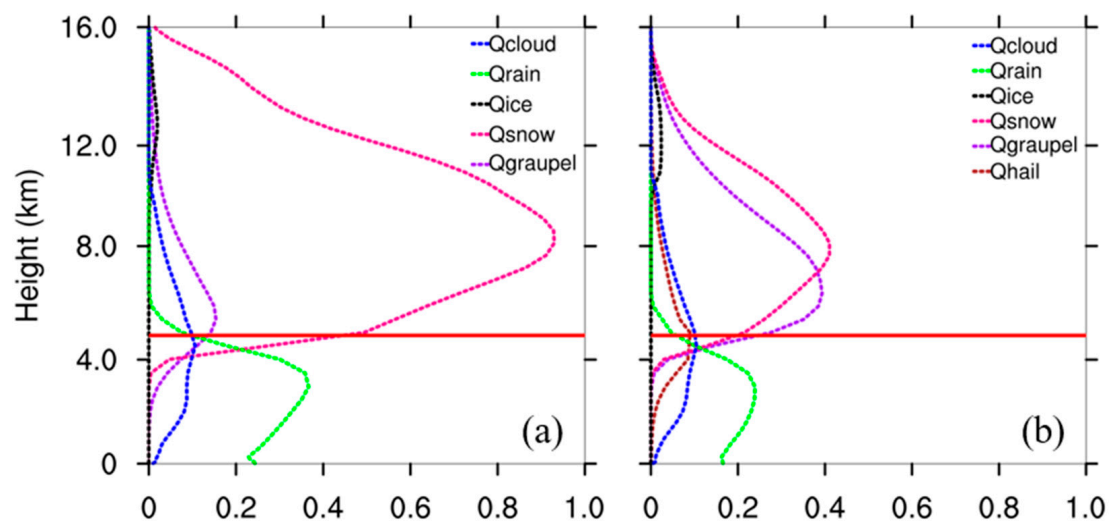


Figure 5. Vertical distribution of the regional averaged hydrometeor mixing ratios (units: g kg^{-1}) at the mature stage for the two schemes, with (a) for the THOM scheme and (b) for the MY scheme. The red solid line indicates the $0\text{ }^{\circ}\text{C}$ isothermal layer.

For the MY scheme, it can be found that the strong radar reflectivity regions above the $0\text{ }^{\circ}\text{C}$ level in the convective zone are primarily contributed by graupel and hail particles. Therefore, the differences in the heights of the strong radar reflectivity regions between the two schemes are due to the different vertical distribution of graupel and hail particles. Below the $0\text{ }^{\circ}\text{C}$ level, the distribution characteristics of K_{DP} is mainly contributed by rainwater.

The analysis in this section indicates that the differences between the two schemes, as well as the discrepancies between radar observations and simulation results, mainly arise from the variations in raindrops and graupel/hail particles. The next section will analyze the source and sink terms of raindrop particles and graupel/hail particles to elucidate the specific reasons for these differences.

3.2.2. Analysis of the Source and Sink Term for Rainwater and Graupel/Hail Particles

To compare the main microphysical processes related to rain and graupel/hail particles for the two schemes, Figure 6a,b display the average tendency of raindrops during the mature stage, while Figure 6c–e show the equivalent for graupel/hail particles. As can be inferred from Figure 6a,b, between the $0\text{ }^{\circ}\text{C}$ level and 2 km in altitude, the raindrop evaporation process is weaker (qr_{rev} in the Figure 6a), and the production and growth of raindrops are mainly due to the melting of graupel and snow particles (qr_{sml} & qr_{gml} in the Figure 6a), as well as the collection of graupel and cloud water (qr_{rcg} & qr_{rcc} in the Figure 6a) by raindrops in THOM. In the same altitude range, the production and growth of raindrops in the MY scheme also rely on the melting of ice-phase particles such

as graupel, hail, and snow (qr_gml & qr_hml & qr_sml in the Figure 6b), and the collection of cloud water by raindrops (qr_rcc in the Figure 6b). At the same time, the rate of hail collecting raindrops (qr_rch in the Figure 6b) and the evaporation of raindrops (qr_rev in the Figure 6b) also increase with decreasing altitude, but the source term rate of raindrops is significantly greater than the sink term. Between 2 km and the ground level, in the THOM scheme, graupel and snow particles are almost completely melted (qr_sml & qr_gml in the Figure 6a), and the rate of raindrops collecting graupel particles (qr_rcg in the Figure 6a) and the collection of cloud droplets by raindrops (qr_rcc in the Figure 6a) all decrease with altitude decreasing, while the evaporation rate of raindrops (qr_rev in the Figure 6a) first increases and then slowly decreases with decreasing altitude. The source term rate is less than the sink term rate, leading to a decrease in the rain mixing ratio with decreasing height. As a result, both schemes produced similar surface precipitation.

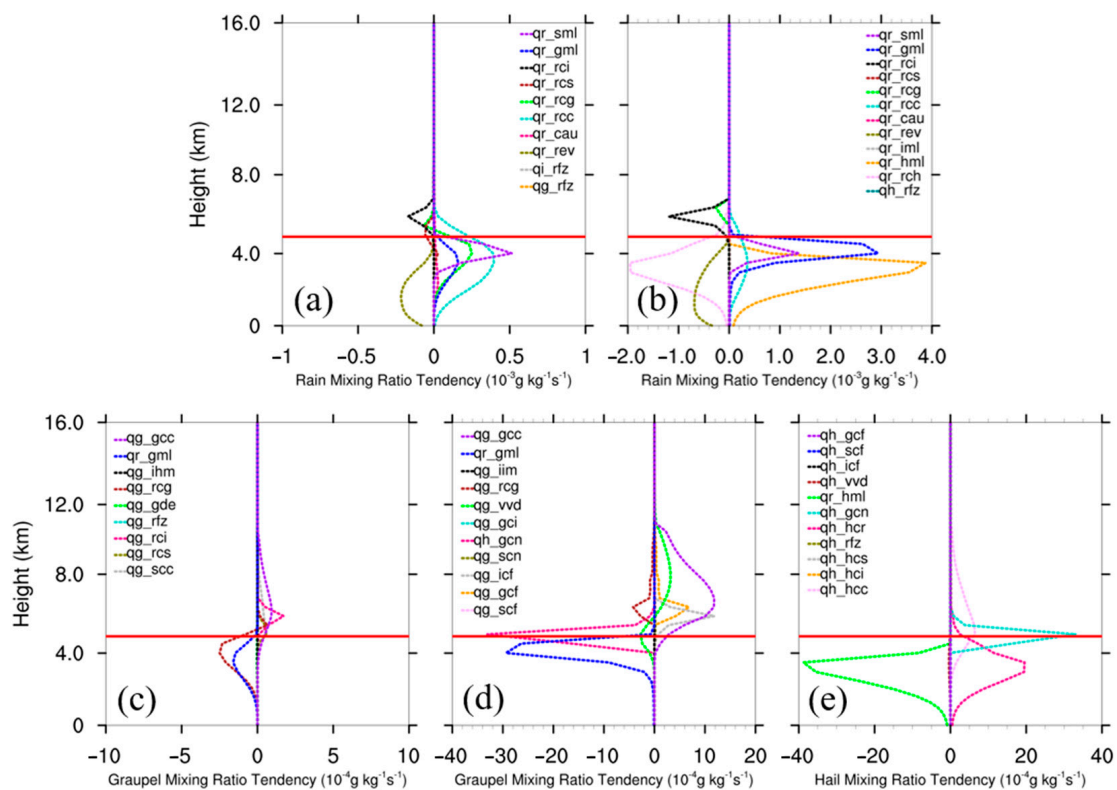


Figure 6. Vertical distribution of the mean tendency of rain and graupel/hail mixing ratios (units: $g\ kg^{-1}$) during the mature stage for the two schemes; (a) for raindrops in THOM, and (b) for raindrops in MY, (c) for graupel particles in THOM, (d) for graupel particles in MY, (e) for hail particles in MY. The red solid line indicates the $0\ ^\circ C$ isothermal layer. The full names of microphysical processes are listed in the Appendix A Tables A1 and A2.

Similarly, in MY, between 2 km and the surface level, the main source terms for raindrops are the melting of hail and the collection of cloud water by raindrops (qr_hml & qr_rcc in the Figure 6b), while the main sink terms are the collection of hail particles by raindrops (qr_rch in the Figure 6b) and the evaporation of raindrops (qr_rev in the Figure 6b). In this case, the source term rate is also less than the sink term rate, resulting in a decrease in the rain mixing ratio with decreasing height. Consistent with Figures 5 and 6, similar to the distribution trend of raindrops content with height, the K_{DP} also shows a trend of increasing first and then decreasing with the decrease in height.

Above 8 km in altitude, the growth of THOM graupel particles is primarily due to the collection of cloud droplets (qg_gcc in the Figure 6c). The growth of MY graupel particles is mainly influenced by the combined action of collecting cloud droplets (qg_gcc

in the Figure 6d) and the deposition of water vapor (qg_vvd in the Figure 6d). The growth of MY hail particles is mainly from the collection of cloud droplets (qh_hcc in the Figure 6e). Comparisons of the two schemes indicate that graupel/hail particles of MY has a significantly higher growth rate above 8 km in altitude than THOM, consistent with the more graupel/hail particles above 8 km in altitude (Figure 5) and the more intensified radar reflectivity above freezing level in MY schemes.

3.2.3. Characteristics of Cold Pool

Figure 7 shows the potential temperature at a 540 m height during the mature stage for both schemes. It is noteworthy that the spatial distributions of the cold pool simulated by the two schemes are similar, which contrasts with the usual outcome in previous studies where different microphysical schemes typically lead to distinct thermodynamic structures [17,50]. However, this does not imply that the impact of microphysical processes on the cold pool is negligible.

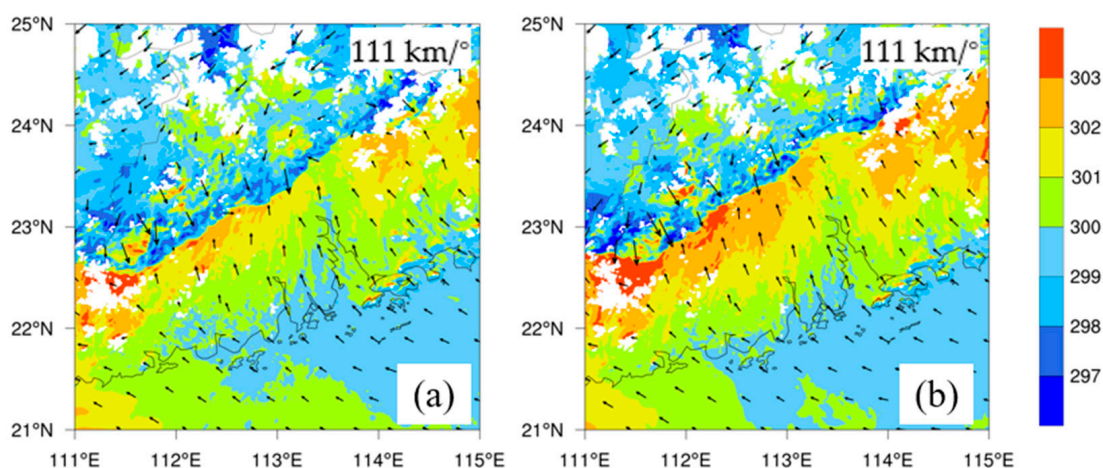


Figure 7. Horizontal cross-sections of potential temperature (units: K) at 540 m simulated by the THOM (a) and MY (b) schemes, respectively. The black arrows indicate the horizontal wind field.

3.2.4. Analysis of Raindrop Mass-Weighted Diameter

In 2M microphysics schemes, the evaporation rate is closely tied to the raindrop size distribution [38,41], which is crucial for the formation of cold pools [24,39]. Zhou et al. [51] highlighted the importance of cold pool evolution for the development of bow echoes based on observational data analysis. This section will analyze the impact of $D_{m,r}$ on the simulation of cold pools. As shown in Figure 8, $D_{m,r}$ distribution in THOM is similar to that in MY, with the majority of raindrop diameter below the $0\text{ }^{\circ}\text{C}$ level being between 0 and 2 mm, and a small fraction of raindrops with $D_{m,r}$ larger than 2 mm. Below the $0\text{ }^{\circ}\text{C}$ level, the Z_{DR} in THOM and MY is greater than the observed values, indicating that THOM and MY overestimate the raindrop sizes (Figure 3(a3–c3)). Since THOM simulates the overall structure of the convective cloud evolution and the accumulated precipitation more closely to observations, the next section will further explore the possible mechanisms and pathways to improve the simulation of $D_{m,r}$ and radar polarimetric quantities in THOM.

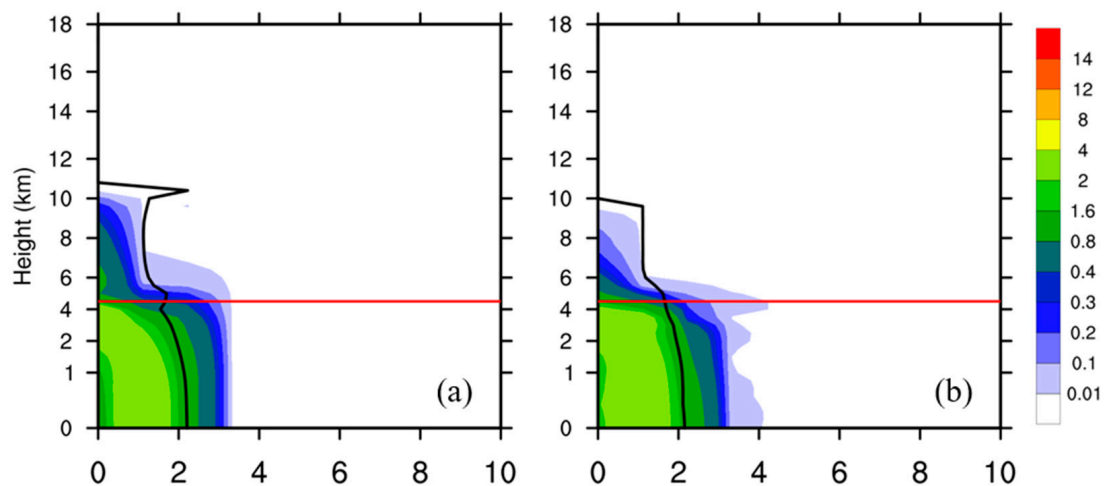


Figure 8. Probability Density Function (PDF) distribution of the simulated $D_{m,r}$ (units: mm) from the THOM (a) and MY (b) schemes. The solid black line indicates the vertical profile of the mean $D_{m,r}$, while the solid red line denotes the 0 °C isotherm.

4. Sensitivity Experiments

Previous studies have shown that the evaporation of raindrops, which can produce or intensify cold pools, have significant impacts on the lifecycle of convection [9,19]. Meanwhile, changes in the size distribution or spectrum caused by raindrop breakup may alter evaporation, thus affecting the cold pool [23–25]. The comparison of the simulated and the observed Z_{DR} found that both schemes' default settings overestimated raindrop sizes (Figure 3(a3–c3)).

It is found that the evaporation process rapidly depletes small raindrops, thereby increasing the $D_{m,r}$, whereas the breakup process, due to the transformation of large raindrops into smaller ones, tends to decrease the $D_{m,r}$ [52]. From Figure 8, it can be seen that simulation results of MY exhibit a consistent increase in the $D_{m,r}$ below the 0 °C level, where THOM shows a pattern of first decreasing and then increasing $D_{m,r}$ below the 0 °C level.

Based on the aforementioned analysis, sensitivity experiments were conducted in THOM to specifically address the raindrop breakup and evaporation processes. For the raindrop breakup process, we modified the threshold diameter D_b in the coalescence-breakup efficiency (Appendix B Formula (A1)) of the THOM scheme. D_b is the threshold diameter for initiating breakup, modifying D_b directly impacts the raindrop size distribution, which in turn affects the evaporation process, and for the raindrop evaporation processes, we directly modified the evaporation efficiency E_E (Appendix B Formula (A2)) by multiplying it by different factors. The alteration in E_E has a direct impact on the evaporation process of rainwater.

As shown in Table 2, for the raindrop breakup process, six simulations were conducted with D_b set at 1.0, 1.2, 1.4, 1.6, 1.8, and 2.2 mm, respectively (THOM_BKP1000, THOM_BKP1200, THOM_BKP1400, THOM_BKP1600, THOM_BKP1800, THOM_BKP2200). For the raindrop evaporation process, similar to Qian et al. [17], five simulations were conducted by directly multiplying the evaporation efficiency E_E by 0.5, 1.5, 3.0, 5.0, and 10.0, respectively (THOM_EVP0.5, THOM_EVP1.5, THOM_EVP3.0, THOM_EVP5.0, THOM_EVP10.0). For comparison, the original THOM simulation will be referred to as THOM_CTR in the following text.

Figure 9 presents a PDF of the difference in simulated $D_{m,r}$ between sensitivity experiments and THOM_CTR during the mature stage. Overall, for the BKP tests, as D_b decreases, the proportion of raindrops $D_{m,r}$ larger than 2 mm decreases, while the proportion of smaller raindrops ($D_{m,r}$ is 0–2 mm) increases, indicating an enhanced raindrop breakup process (Figure 9(a1–e1)); as D_b increases, it has little impact on raindrops $D_{m,r}$ larger than 2 mm (Figure 9(f1)). As for the EVP experiments, for the simulations with increased E_E ,

due to the substantial evaporation of smaller raindrops ($D_{m,r}$ is 0–1 mm), the proportion of raindrops $D_{m,r}$ larger than 1mm below the freezing layer increases (Figure 9(b2–e2)); conversely, the situation with a decrease in E_E is just the opposite (Figure 9(a2)). This phenomenon suggests that decreasing D_b and decreasing E_E can generate more smaller raindrops, while increasing E_E will enhance the proportion of larger raindrops.

Table 2. Introduction to sensitivity experiments.

Modified Variables	The Name of Sensitivity Experiments
D_b (1.95 mm)	THOM_BKP1000, THOM_BKP1200, THOM_BKP1400, THOM_BKP1600, THOM_BKP1800, THOM_BKP2200
E_E	THOM_EVP0.5, THOM_EVP1.5, THOM_EVP3.0, THOM_EVP5.0, THOM_EVP10.0

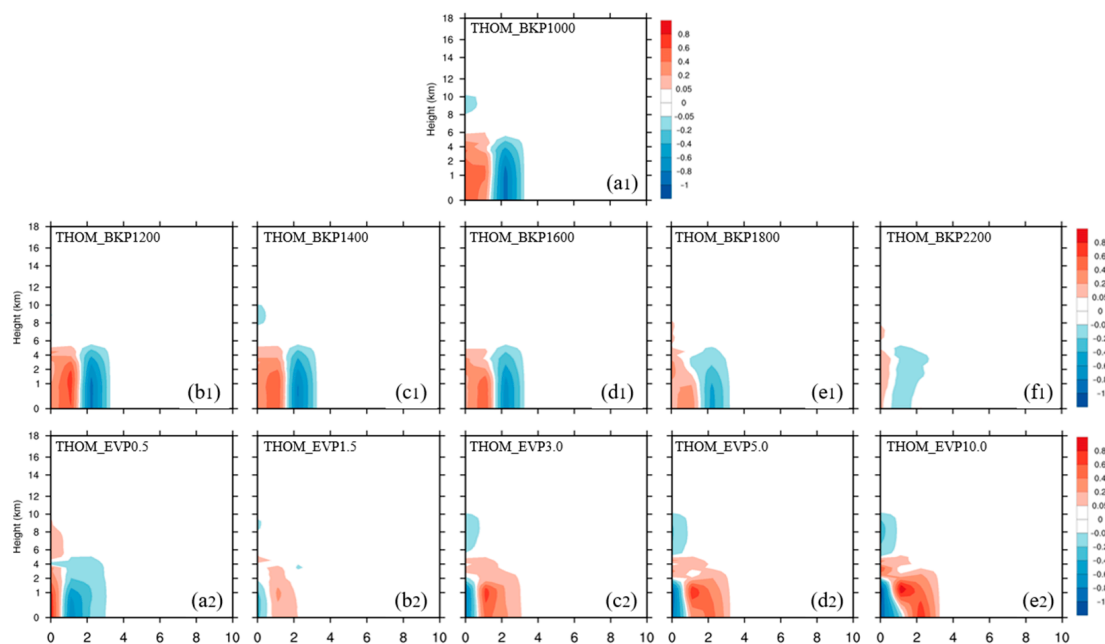


Figure 9. A PDF of the difference in simulated $D_{m,r}$ between sensitivity experiments and THOM_CTRL during the mature stage of the convection. Panels (a1–f1) display the results of the BKP experiments, while panels (a2–e2) show the outcomes of the EVP experiments.

Figure 10(a1–f1, a2–e2) illustrate the difference of cold pools between two sets of sensitivity experiments and the THOM_CTRL. As expected, the reduction of D_b in the BKP experiments (enhancing breakup efficiency) led to the production of smaller raindrops (Figure 9(a1–e1)), resulting in higher rates of rain evaporation and stronger cold pools (Figure 10(a1–e1)). However, only in THOM_BKP1000, modifying the breakup parameters significantly affected the intensity and extent of the cold pool, and its particle size distribution already diverged significantly from THOM_CTRL (Figure 8a). This suggests that modifying the raindrop breakup process not only improves the mass-weighted diameter distribution, but also leads to a substantial increase in cold pool intensity or extent. Regarding the EVP experiments, there were significant changes in both cold pool intensity and extent across all five simulations, particularly evident in THOM_EVP0.5 and THOM_EVP3.0 (Figure 10(a2–e2)). The transition from THOM_EVP3.0 to THOM_EVP5.0 and then to THOM_EVP10.0 showed only marginal changes in the cold pool.

As shown in Figure 5a, raindrops are primarily located below 4 km in altitude. The observation indicates that Z_{DR} is mainly distributed between 0 and 1 dB at altitudes below 4 km (Figure 11a). Compared to THOM_CTRL, where Z_{DR} is mainly distributed between 0 and 3 dB (Figure 11b), THOM_BKP1000 shows Z_{DR} values more closely aligned with

observations (Figure 11c), concentrated between 0 and 1 dB below 4 km. Therefore, we believe that reducing D_b can better improve the simulation results.

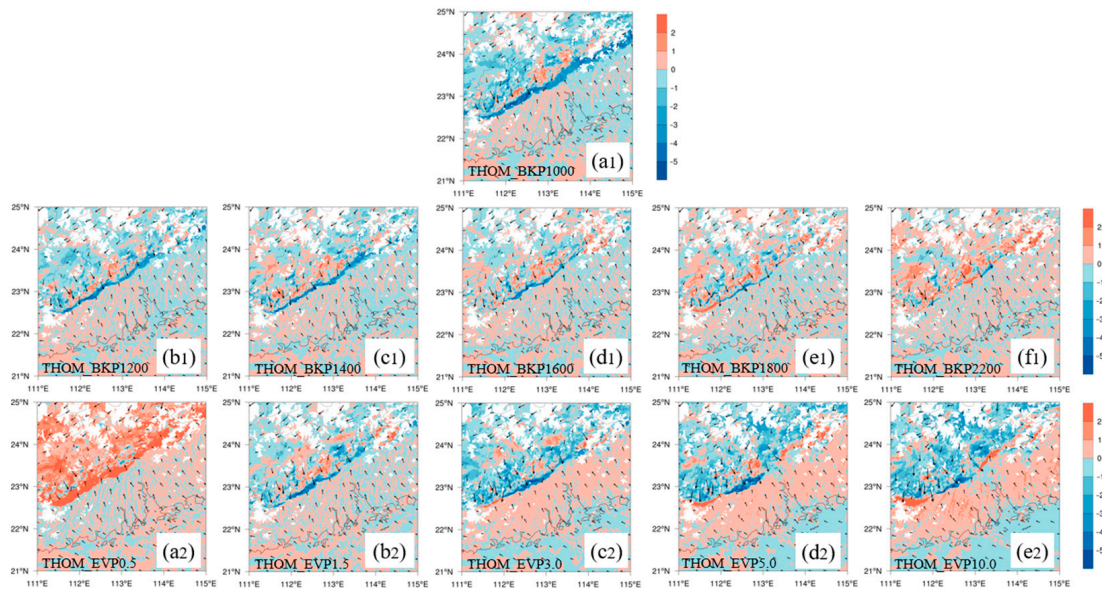


Figure 10. Horizontal cross-sections of the difference in simulated potential temperature (units: K) between sensitivity experiments and THOM_CTRL at an altitude of 540m during the mature stage, with the results of the BKP tests (a1–f1) and the results of the EVP tests (a2–e2). The black arrows represent the horizontal wind field.

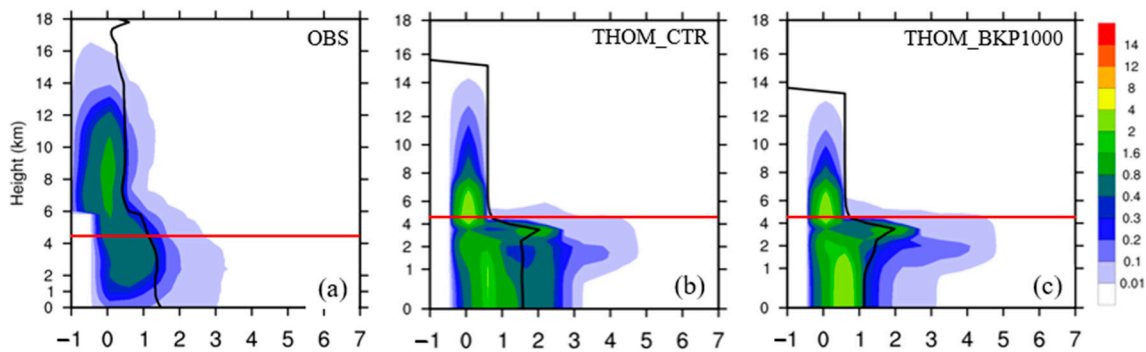


Figure 11. A PDF of the Z_{DR} (units: dB) by the OBS (a), THOM_CTRL (b), and THOM_BKP1000 (c) during the mature stage. The solid red line denotes the 0 °C isotherm.

5. Discussion

In recent years, dual-polarization radar has been used to compare the microphysical characteristics of heavy rainfall between observations and NWP models in order to improve the microphysical schemes within the models [28,53–55]. Zhou et al. [26] pointed out that the default settings of microphysics schemes used in the WRF model that was primarily designed based on the environmental characteristics of North America produced poor simulation results in southeastern China. With three 2M schemes (THOM, Morrison, and WDM6) employed, it is shown that both THOM and WDM6 underestimated K_{DP} and Z_{DR} , while Morrison significantly overestimated them. Increasing the coalescence-breakup and evaporation efficiencies in THOM improved the simulation results. Sun et al. [56] compared the polarimetric radar variables and corresponding hydrometeor types derived from the WRF model and radar simulator, and conducted radar observations and retrievals of a strong squall line over central China. By comparing Z_{DR} and K_{DP} , it was found that the Morrison and WDM6 schemes simulated a lower proportion of large

raindrops and lower liquid water content in the convective region [56]. Zhou et al. [57] simulated a heavy precipitation process in Guangdong, with the three 2M microphysics schemes (Morrison, THOM, and MY), overestimated K_{DP} and Z_{DR} , and raindrops' mass-weighted mean diameter ($D_{m,r}$). Reducing the coalescence-break efficiency in the MY scheme led to better simulation results after the initial stage [57]. These studies indicate that dual-polarization radar plays a crucial role in evaluating and improving microphysics schemes in models.

6. Conclusions

In this study, we utilized the S-band dual-polarization radar parameters (Z_H , K_{DP} , Z_{DR}) located in Guangzhou, and conducted a simulation analysis of a severe convective precipitation process in Guangdong on 8 May 2017 using the THOM and MY microphysical schemes in a WRF model. The outputs from WRFv4.2 were transformed into simulated radar polarization parameters by use of the CAPS-PRS radar simulator. The aim of this study was to deepen our understanding of the impact of microphysical processes on the development and evolution of convective systems in models through the investigation of parameterizations of raindrop breakup and evaporation.

Key conclusions obtained are as follows:

(1) The THOM scheme produced more snow crystals, while the MY scheme produced more graupel particles. The total ice water content of both schemes was very close. The ice-phase particles of both schemes melted rapidly below the 0 °C level and had similar evaporation efficiencies, resulting in comparable surface precipitation.

(2) The simulated vertical cross-section of Z_H from THOM was closer to the observations than MY. It is shown that THOM's simulation of the strong radar reflectivity region in the convective area was closer to the observations, which is due to the graupel/hail particles simulated by the MY scheme that exists at higher altitudes.

From the source and sink terms in two schemes, it is evident that the increase in the liquid water mixing ratio below the 0 °C level primarily originates from the melting of the ice-phase particle. Between the 0 °C level and 2 km in altitude, almost all ice-phase particles have melted. Below 2 km in altitude, the liquid water mixing ratio decreases primarily due to evaporation. Therefore, the differences between the simulated and the observed K_{DP} between the melting layer and 2 km in altitude may be due to the default settings of the raindrop evaporation or breakup parameterization schemes.

(3) Compared to the observations of Z_{DR} , the simulations produced overestimated the raindrop size. This discrepancy suggests that the relatively lower efficiency of raindrop breakup in the default settings of the THOM may be the contributing factors. To further investigate the impact of microphysical processes on raindrop size distributions and cold pool dynamics, two sets of numerical experiments were conducted, focusing on modifying the breakup diameter threshold (D_b) and the evaporation efficiency (E_E) to assess their effects on $D_{m,r}$ and cold pool, respectively. It was found that adjusting D_b significantly changed the simulated raindrop size distribution, and had a certain impact on the strength of cold pool, whereas modifying E_E significantly not only changed the intensity and scope of the cold pool, but also had great effect on the $D_{m,r}$. We then compared the Z_{DR} from the sensitivity experiments with those observed and found that reducing D_b can cause Z_{DR} to concentrate within the 0–1 dB range (consistent with observations) and THOM_BKP1000 most closely matched the observations. Therefore, we conclude that reducing D_b can produce better simulation results of Z_{DR} .

The schematic diagram of the potential impact of droplet breakup and evaporation on convective development can be shown in Figure 12. After the decrease/increase in D_b , more/fewer small raindrops will be generated, and the intensity and extent of the cold pool will slightly increase/decrease, subsequently affecting the strengthening/weakening of downdrafts/updrafts. The increase/decrease in E_E has little effect on raindrop size, but it significantly enhances/weakens the intensity and extent of the cold pool, leading to the strengthening of downdrafts/updrafts.

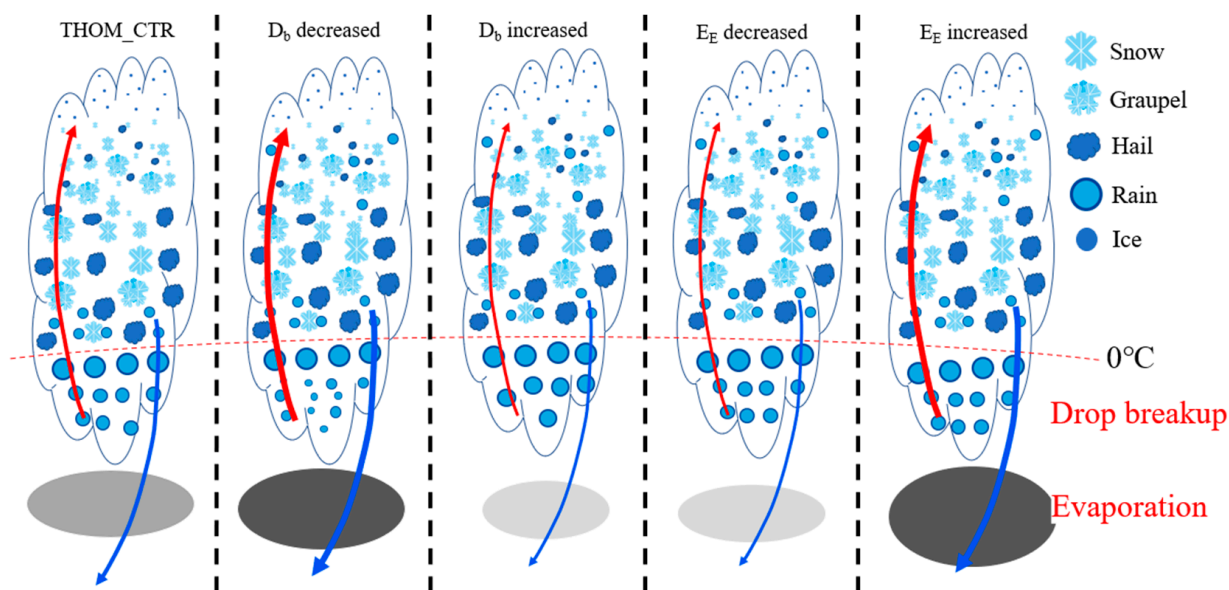


Figure 12. A schematic diagram of the potential impact of droplet breakup and evaporation on convective development, divided into five parts: control group THOM_CTRL, increased/decreased D_b , and increased/decreased E_E . In the figure, the depth of color and size of the grey ellipses represent the intensity and extent of the cold pool, the size of the blue/red arrows indicates the magnitude of the downdraft/updraft, and the red dashed line represents the zero-degree isotherm.

This paper specifically analyzed a severe convective precipitation event under weak synoptic conditions (the 0–6 km vertical wind shears of MCSs in southeast China during PSRS range from 10 to 20 m/s [51,58,59], which is weaker than the North America counterparts of 15–30 m/s [50,60]) and a humid climate in the Guangdong region. Future research should continue to utilize dual-polarization radar to explore the relationship between the formation of bow echoes and the environmental conditions in southeast China. This highlights the complexity of microphysical processes and the need for comprehensive parameter tuning. Our study demonstrates the feasibility of modifying the default microphysics settings of THOM based on polarimetric radar data and a radar simulator to improve the simulation of MCSs in southeast China. However, the effectiveness of this approach needs to be confirmed through additional case studies to refine the simulation and forecasting of MCSs in this region.

Author Contributions: Writing—original draft, Z.C.; Writing—review & editing, X.L. All authors have read and agreed to the published version of the manuscript.

Funding: This research was funded by the National Natural Science Foundation of China (Grant Nos. 41975176, 42061134009).

Data Availability Statement: The data presented in this study are available on request from the author.

Acknowledgments: We acknowledge the High Performance Computing Platform of Nanjing University of Information Science and Technology for their support of this work. Moreover, this study was supported by the National Key Scientific and Technological Infrastructure project Earth System Numerical Simulation Facility (EarthLab).

Conflicts of Interest: The authors declare no conflict of interest.

Appendix A

Table A1. THOM source and sink terms and full names of microphysical processes.

Self-Named Titles	Original Titles	Microphysical Process
qg_gcc	prg_gcw	Graupel collecting cloud water.
qr_gml	prr_gml	Graupel melting into rain.
qg_ihm	prg_ihm	Ice multiplication from rime-splinters.
qg_rcg	prg_rcg	Rain collecting graupel.
qg_gde	prg_gde	Deposition/sublimation of graupel.
qg_rfz	prg_rfz	Rain freezing into graupel.
qg_rci	prg_rci	Ice collecting rain into graupel.
qg_rcs	prg_rcs	Snow collecting rain into graupel.
qg_scc	prg_scv	Snow collecting cloud water into graupel.
qr_sml	prr_sml	Snow melting into rain.
qr_rci	prr_rci	Rain collecting ice.
qr_rcs	prr_rcs	Rain collecting snow.
qr_rcg	prr_rcg	Rain collecting graupel.
qr_rcc	prr_rcw	Rain collecting cloud water.
qr_cau	prr_wau	Autoconversion.
qr_rev	prv_rev	Rain evaporation.
qi_rfz	pri_rfz	Rain freezing into ice.

Table A2. MY source and sink terms and full names of microphysical processes.

Self-Named Titles	Original Titles	Microphysical Process
qg_gcc	QCLcg	Graupel collecting cloud water.
qr_gml	QMLgr	Graupel melting into rain.
qg_iim	QIMgi	Ice multiplication from rime-splinters.
qg_rcg	QCLgr	Rain collecting graupel.
qg_vvd	QVDvg	Deposition/sublimation of graupel.
qg_gci	QCLig	Graupel collecting ice.
qh_gcn	QCNgh	Graupel converting to hail.
qg_scn	QCNsg	Snow converting to graupel.
qg_icf	Dirg*(QCLir+QCLri)	3-comp.freezing into graupel.
qg_gcf	Dgrg*(QCLgr+QCLrg)	3-comp.freezing into graupel.
qg_scf	Dsrg*(QCLsr+QCLrs)	3-comp.freezing into graupel.
qh_gcf	Dgrh*(QCLgr+QCLrg)	3-comp.freezing into hail.
qh_scf	Dsrh*(QCLsr+QCLrs)	3-comp.freezing into hail.
qh_icf	Dirh*(QCLir+QCLri)	3-comp.freezing into hail.
qh_vvd	QVDvh	Deposition/sublimation of hail.
qr_hml	QMLhr	Hail melting into rain.
qh_hcr	QCLrh	Hail collecting rain.
qh_rfz	QFZrh	Rain freezing into hail.
qh_hcs	QCLsh	Hail collecting snow.
qh_hci	QCLih	Hail collecting ice.
qh_hcc	QCLch	Hail collecting cloud water.
qr_sml	QMLsr	Snow melting into rain.
qr_gml	QMLgr	Graupel melting into rain.
qr_rci	QCLri	Rain collecting ice.
qr_icr	QCLir	Ice collecting rain.
qr_rcs	QCLrs	Rain collecting snow.
qr_scr	QCLsr	Snow collecting rain.
qr_rcg	QCLrg	Rain collecting graupel.
qr_gcr	QCLgr	Graupel collecting rain.
qr_rcc	RCACCR	Rain collecting cloud water.
qr_cau	RCAUTR	Autoconversion.

Table A2. Cont.

Self-Named Titles	Original Titles	Microphysical Process
qr_rev	QREVP	Rain evaporation.
qr_uml	QMLir	Ice melting into rain.
qr_rch	QCLrh	Rain collecting hail.
qh_rfz	QFZrh	Freezing water drops into hail.

*: multiplication sign; 3-comp.: three types of hydrometeors are involved.

Appendix B

For the raindrop breakup process, the coalescence-breakup efficiency in THOM was defined based on the formula proposed by Verlinde & Cotton [61]:

$$E_C = 2 - \exp\left[2.3 \times 10^6 \times (D_m - D_b)\right], D_m > 0.05 \text{ mm} \quad (\text{A1})$$

where E_C represents the rain coalescence-breakup efficiency, and D_b (mm) is the threshold diameter for initiating breakup. In THOM, the default value for D_b is set at 1.95 mm.

For the raindrop evaporation process, the THOM model follows the Formula (16) from Srivastava & Coen [62], where the evaporation efficiency is given by:

$$E_E = 2\pi(S - 1)f\left(N_0f(\lambda)f(\rho)f(V_{fall})\right)CP_{92}, \quad (\text{A2})$$

where S represents the air supersaturation, $f(X)$ denotes the relationship between E_E and X , ρ is the air density, V_{fall} is a parameter for the raindrop fall velocity, and CP_{92} refers to certain thermodynamic and nucleation dynamics parameters.

References

- Luo, Y. Advances in Understanding the Early-Summer Heavy Rainfall over South China. In *World Scientific Series on Asia-Pacific Weather and Climate*; World Scientific: Singapore, 2017; Volume 9, pp. 215–226, ISBN 978-981-320-090-6.
- Guo, J.; Feng, T.; Cai, Z.; Lian, X.; Tang, W. Vulnerability Assessment for Power Transmission Lines under Typhoon Weather Based on a Cascading Failure State Transition Diagram. *Energies* **2020**, *13*, 3681. [\[CrossRef\]](#)
- Wang, L.; Dong, Y.; Zhang, C.; Heng, Z. Extreme and Severe Convective Weather Disasters: A Dual-Polarization Radar Nowcasting Method Based on Physical Constraints and a Deep Neural Network Model. *Atmos. Res.* **2023**, *289*, 106750. [\[CrossRef\]](#)
- Cao, X.; Qi, Y.; Ni, G. X-Band Polarimetric Radar QPE for Urban Hydrology: The Increased Contribution of High-Resolution Rainfall Capturing. *J. Hydrol.* **2023**, *617*, 128905. [\[CrossRef\]](#)
- Chao, L.; Zhang, K.; Yang, Z.-L.; Wang, J.; Lin, P.; Liang, J.; Li, Z.; Gu, Z. Improving Flood Simulation Capability of the WRF-Hydro-RAPID Model Using a Multi-Source Precipitation Merging Method. *J. Hydrol.* **2021**, *592*, 125814. [\[CrossRef\]](#)
- Wang, S.; Zhang, K.; Chao, L.; Li, D.; Tian, X.; Bao, H.; Chen, G.; Xia, Y. Exploring the Utility of Radar and Satellite-Sensed Precipitation and Their Dynamic Bias Correction for Integrated Prediction of Flood and Landslide Hazards. *J. Hydrol.* **2021**, *603*, 126964. [\[CrossRef\]](#)
- Luo, L.; Xue, M.; Zhu, K.; Zhou, B. Explicit Prediction of Hail Using Multimoment Microphysics Schemes for a Hailstorm of 19 March 2014 in Eastern China. *JGR Atmos.* **2017**, *122*, 7560–7581. [\[CrossRef\]](#)
- Morrison, H.; Van Lier-Walqui, M.; Fridlind, A.M.; Grabowski, W.W.; Harrington, J.Y.; Hoose, C.; Korolev, A.; Kumjian, M.R.; Milbrandt, J.A.; Pawlowska, H.; et al. Confronting the Challenge of Modeling Cloud and Precipitation Microphysics. *J. Adv. Model. Earth Syst.* **2020**, *12*, e2019MS001689. [\[CrossRef\]](#)
- Bao, J.-W.; Michelson, S.A.; Grell, E.D. Microphysical Process Comparison of Three Microphysics Parameterization Schemes in the WRF Model for an Idealized Squall-Line Case Study. *Mon. Weather Rev.* **2019**, *147*, 3093–3120. [\[CrossRef\]](#)
- Khain, A.P.; Beheng, K.D.; Heymsfield, A.; Korolev, A.; Krichak, S.O.; Levin, Z.; Pinsky, M.; Phillips, V.; Prabhakaran, T.; Teller, A.; et al. Representation of Microphysical Processes in Cloud-resolving Models: Spectral (Bin) Microphysics versus Bulk Parameterization. *Rev. Geophys.* **2015**, *53*, 247–322. [\[CrossRef\]](#)
- Wu, D.; Dong, X.; Xi, B.; Feng, Z.; Kennedy, A.; Mullendore, G.; Gilmore, M.; Tao, W. Impacts of Microphysical Scheme on Convective and Stratiform Characteristics in Two High Precipitation Squall Line Events. *JGR Atmos.* **2013**, *118*. [\[CrossRef\]](#)
- Wang, H.; Auligné, T.; Morrison, H. Impact of Microphysics Scheme Complexity on the Propagation of Initial Perturbations. *Mon. Weather Rev.* **2012**, *140*, 2287–2296. [\[CrossRef\]](#)
- Zhang, Y.; Yu, H.; Zhang, M.; Yang, Y.; Meng, Z. Uncertainties and Error Growth in Forecasting the Record-Breaking Rainfall in Zhengzhou, Henan on 19–20 July 2021. *Sci. China Earth Sci.* **2022**, *65*, 1903–1920. [\[CrossRef\]](#)

14. Zhu, K.; Zhang, C.; Xue, M.; Yang, N. Predictability and Skill of Convection-Permitting Ensemble Forecast Systems in Predicting the Record-Breaking “21·7” Extreme Rainfall Event in Henan Province, China. *Sci. China Earth Sci.* **2022**, *65*, 1879–1902. [[CrossRef](#)]
15. Simpson, J.E. A Comparison between Laboratory and Atmospheric Density Currents. *Quart. J. R. Meteorol. Soc.* **1969**, *95*, 758–765. [[CrossRef](#)]
16. Morrison, H.; Milbrandt, J.A. Parameterization of Cloud Microphysics Based on the Prediction of Bulk Ice Particle Properties. Part I: Scheme Description and Idealized Tests. *J. Atmos. Sci.* **2015**, *72*, 287–311. [[CrossRef](#)]
17. Qian, Q.; Lin, Y.; Luo, Y.; Zhao, X.; Zhao, Z.; Luo, Y.; Liu, X. Sensitivity of a Simulated Squall Line During Southern China Monsoon Rainfall Experiment to Parameterization of Microphysics. *JGR Atmos.* **2018**, *123*, 4197–4220. [[CrossRef](#)]
18. Drager, A.J.; Van Den Heever, S.C. Characterizing Convective Cold Pools. *J. Adv. Model. Earth Syst.* **2017**, *9*, 1091–1115. [[CrossRef](#)]
19. Langhans, W.; Romps, D.M. The Origin of Water Vapor Rings in Tropical Oceanic Cold Pools. *Geophys. Res. Lett.* **2015**, *42*, 7825–7834. [[CrossRef](#)]
20. Khairoutdinov, M.; Randall, D. High-Resolution Simulation of Shallow-to-Deep Convection Transition over Land. *J. Atmos. Sci.* **2006**, *63*, 3421–3436. [[CrossRef](#)]
21. Weisman, M.L.; Rotunno, R. “A Theory for Strong Long-Lived Squall Lines” Revisited. *J. Atmos. Sci.* **2004**, *61*, 361–382. [[CrossRef](#)]
22. Davis, C.A.; Lee, W.-C. Mesoscale Analysis of Heavy Rainfall Episodes from SoWMEX/TiMREX. *J. Atmos. Sci.* **2012**, *69*, 521–537. [[CrossRef](#)]
23. Morrison, H.; Milbrandt, J. Comparison of Two-Moment Bulk Microphysics Schemes in Idealized Supercell Thunderstorm Simulations. *Mon. Wea. Rev.* **2011**, *139*, 1103–1130. [[CrossRef](#)]
24. Tridon, F.; Planche, C.; Mroz, K.; Banson, S.; Battaglia, A.; Van Baelen, J.; Wobrock, W. On the Realism of the Rain Microphysics Representation of a Squall Line in the WRF Model. Part I: Evaluation with Multifrequency Cloud Radar Doppler Spectra Observations. *Mon. Weather Rev.* **2019**, *147*, 2787–2810. [[CrossRef](#)]
25. Van Weverberg, K.; Vogelmann, A.M.; Morrison, H.; Milbrandt, J.A. Sensitivity of Idealized Squall-Line Simulations to the Level of Complexity Used in Two-Moment Bulk Microphysics Schemes. *Mon. Weather Rev.* **2012**, *140*, 1883–1907. [[CrossRef](#)]
26. Zhou, A.; Zhao, K.; Lee, W.; Ding, Z.; Lu, Y.; Huang, H. Evaluation and Modification of Microphysics Schemes on the Cold Pool Evolution for a Simulated Bow Echo in Southeast China. *JGR Atmos.* **2022**, *127*, e2021JD035262. [[CrossRef](#)]
27. Lompar, M.; Ćurić, M.; Romanić, D. Implementation of a Gust Front Head Collapse Scheme in the WRF Numerical Model. *Atmos. Res.* **2018**, *203*, 231–245. [[CrossRef](#)]
28. Johnson, M.; Jung, Y.; Dawson, D.; Supinie, T.; Xue, M.; Park, J.; Lee, Y.-H. Evaluation of Unified Model Microphysics in High-Resolution NWP Simulations Using Polarimetric Radar Observations. *Adv. Atmos. Sci.* **2018**, *35*, 771–784. [[CrossRef](#)]
29. Wang, M.; Zhao, K.; Pan, Y.; Xue, M. Evaluation of Simulated Drop Size Distributions and Microphysical Processes Using Polarimetric Radar Observations for Landfalling Typhoon Matmo (2014). *JGR Atmos.* **2020**, *125*, e2019JD031527. [[CrossRef](#)]
30. Bringi, V.N.; Chandrasekar, V.; Hubbert, J.; Gorgucci, E.; Randeu, W.L.; Schoenhuber, M. Raindrop Size Distribution in Different Climatic Regimes from Disdrometer and Dual-Polarized Radar Analysis. *J. Atmos. Sci.* **2003**, *60*, 354–365. [[CrossRef](#)]
31. Ryzhkov, A.V.; Zrnica, D.S. *Radar Polarimetry for Weather Observations*; Springer Atmospheric Sciences; Springer International Publishing: Cham, Switzerland, 2019; ISBN 978-3-030-05092-4.
32. Kumjian, M. Principles and Applications of Dual-Polarization Weather Radar. Part I: Description of the Polarimetric Radar Variables. *J. Oper. Meteor.* **2013**, *1*, 226–242. [[CrossRef](#)]
33. Laroche, S. Polarimetric Doppler Weather Radar: Principles and Applications. *Atmos. Res.* **2002**, *63*, 159–160. [[CrossRef](#)]
34. Carr, N.; Kirstetter, P.E.; Gourley, J.J.; Hong, Y. Polarimetric Signatures of Midlatitude Warm-Rain Precipitation Events. *J. Appl. Meteorol. Climatol.* **2017**, *56*, 697–711. [[CrossRef](#)]
35. Ryzhkov, A.; Pinsky, M.; Pokrovsky, A.; Khain, A. Polarimetric Radar Observation Operator for a Cloud Model with Spectral Microphysics. *J. Appl. Meteorol. Climatol.* **2011**, *50*, 873–894. [[CrossRef](#)]
36. Snyder, J.C.; Bluestein, H.B.; Dawson, D.T.; Jung, Y. Simulations of Polarimetric, X-Band Radar Signatures in Supercells. Part II: ZDR Columns and Rings and KDP Columns. *J. Appl. Meteorol. Climatol.* **2017**, *56*, 2001–2026. [[CrossRef](#)]
37. Gao, W.; Xue, L.; Liu, L.; Lu, C.; Yun, Y.; Zhou, W. A Study of the Fraction of Warm Rain in a Pre-Summer Rainfall Event over South China. *Atmos. Res.* **2021**, *262*, 105792. [[CrossRef](#)]
38. Morrison, H.; Thompson, G.; Tatarskii, V. Impact of Cloud Microphysics on the Development of Trailing Stratiform Precipitation in a Simulated Squall Line: Comparison of One- and Two-Moment Schemes. *Mon. Weather Rev.* **2009**, *137*, 991–1007. [[CrossRef](#)]
39. Dawson, D.T.; Xue, M.; Milbrandt, J.A.; Yau, M.K. Comparison of Evaporation and Cold Pool Development between Single-Moment and Multimoment Bulk Microphysics Schemes in Idealized Simulations of Tornadic Thunderstorms. *Mon. Weather Rev.* **2010**, *138*, 1152–1171. [[CrossRef](#)]
40. Wang, H.; Kong, F.; Wu, N.; Lan, H.; Yin, J. An Investigation into Microphysical Structure of a Squall Line in South China Observed with a Polarimetric Radar and a Disdrometer. *Atmos. Res.* **2019**, *226*, 171–180. [[CrossRef](#)]
41. Thompson, G.; Field, P.R.; Rasmussen, R.M.; Hall, W.D. Explicit Forecasts of Winter Precipitation Using an Improved Bulk Microphysics Scheme. Part II: Implementation of a New Snow Parameterization. *Mon. Weather Rev.* **2008**, *136*, 5095–5115. [[CrossRef](#)]
42. Milbrandt, J.A.; Yau, M.K. A Multimoment Bulk Microphysics Parameterization. Part II: A Proposed Three-Moment Closure and Scheme Description. *J. Atmos. Sci.* **2005**, *62*, 3065–3081. [[CrossRef](#)]

43. Jung, Y.; Xue, M.; Zhang, G. Simulations of Polarimetric Radar Signatures of a Supercell Storm Using a Two-Moment Bulk Microphysics Scheme. *J. Appl. Meteorol. Climatol.* **2010**, *49*, 146–163. [[CrossRef](#)]
44. Hubbert, J.; Brangi, V.N.; Carey, L.D.; Bolen, S. CSU-CHILL Polarimetric Radar Measurements from a Severe Hail Storm in Eastern Colorado. *J. Appl. Meteor.* **1998**, *37*, 749–775. [[CrossRef](#)]
45. Loney, M.L. Enhanced Polarimetric Radar Signatures above the Melting Level in a Supercell Storm. *J. Appl. Meteorol.* **2002**, *41*, 1179–1194. [[CrossRef](#)]
46. Putnam, B.J.; Xue, M.; Jung, Y.; Zhang, G.; Kong, F. Simulation of Polarimetric Radar Variables from 2013 CAPS Spring Experiment Storm-Scale Ensemble Forecasts and Evaluation of Microphysics Schemes. *Mon. Weather Rev.* **2017**, *145*, 49–73. [[CrossRef](#)]
47. Han, B.; Fan, J.; Varble, A.; Morrison, H.; Williams, C.R.; Chen, B.; Dong, X.; Giangrande, S.E.; Khain, A.; Mansell, E.; et al. Cloud-Resolving Model Intercomparison of an MC3E Squall Line Case: Part II. Stratiform Precipitation Properties. *JGR Atmos.* **2019**, *124*, 1090–1117. [[CrossRef](#)]
48. Han, M.; Braun, S.A.; Matsui, T.; Williams, C.R. Evaluation of Cloud Microphysics Schemes in Simulations of a Winter Storm Using Radar and Radiometer Measurements. *JGR Atmos.* **2013**, *118*, 1401–1419. [[CrossRef](#)]
49. Wheatley, D.M.; Yussouf, N.; Stensrud, D.J. Ensemble Kalman Filter Analyses and Forecasts of a Severe Mesoscale Convective System Using Different Choices of Microphysics Schemes. *Mon. Weather Rev.* **2014**, *142*, 3243–3263. [[CrossRef](#)]
50. Fan, J.; Han, B.; Varble, A.; Morrison, H.; North, K.; Kollias, P.; Chen, B.; Dong, X.; Giangrande, S.E.; Khain, A.; et al. Cloud-resolving Model Intercomparison of an MC3E Squall Line Case: Part I—Convective Updrafts. *JGR Atmos.* **2017**, *122*, 9351–9378. [[CrossRef](#)]
51. Zhou, A.; Zhao, K.; Lee, W.; Huang, H.; Hu, D.; Fu, P. VDRAS and Polarimetric Radar Investigation of a Bow Echo Formation After a Squall Line Merged With a Preline Convective Cell. *JGR Atmos.* **2020**, *125*, e2019JD031719. [[CrossRef](#)]
52. Kumjian, M.R.; Lebo, Z.J.; Morrison, H.C. On the Mechanisms of Rain Formation in an Idealized Supercell Storm. *Mon. Weather Rev.* **2015**, *143*, 2754–2773. [[CrossRef](#)]
53. Barnes, H.C.; Houze, R.A. Comparison of Observed and Simulated Spatial Patterns of Ice Microphysical Processes in Tropical Oceanic Mesoscale Convective Systems. *JGR Atmos.* **2016**, *121*, 8269–8296. [[CrossRef](#)]
54. Kumjian, M.R.; Mishra, S.; Giangrande, S.E.; Toto, T.; Ryzhkov, A.V.; Bansemer, A. Polarimetric Radar and Aircraft Observations of Saggy Bright Bands during MC3E. *J. Geophys. Res. Atmos.* **2016**, *121*, 3584–3607. [[CrossRef](#)]
55. Putnam, B.J.; Xue, M.; Jung, Y.; Snook, N.; Zhang, G. The Analysis and Prediction of Microphysical States and Polarimetric Radar Variables in a Mesoscale Convective System Using Double-Moment Microphysics, Multinetwork Radar Data, and the Ensemble Kalman Filter. *Mon. Weather Rev.* **2014**, *142*, 141–162. [[CrossRef](#)]
56. Sun, Y.; Zhou, Z.; Gao, Q.; Li, H.; Wang, M. Evaluating Simulated Microphysics of Stratiform and Convective Precipitation in a Squall Line Event Using Polarimetric Radar Observations. *Remote Sens.* **2023**, *15*, 1507. [[CrossRef](#)]
57. Zhou, Z.; Du, M.; Hu, Y.; Kang, Z.; Yu, R.; Guo, Y. An Evaluation and Improvement of Microphysical Parameterization for a Heavy Rainfall Process during the Meiyu Season. *Remote Sens.* **2024**, *16*, 1636. [[CrossRef](#)]
58. Wan, Q.; Wang, B.; Wong, W.K.; Hu, Z.; Jou, B.J.-D.; Lin, Y.; Johnson, R.H.; Chang, C.-P.; Zhu, Y.; Zhang, X.; et al. The Southern China Monsoon Rainfall Experiment (SCMREX). *Bull. Am. Meteorol. Soc.* **2017**, *98*, 999–1013. [[CrossRef](#)]
59. Meng, Z.; Yan, D.; Zhang, Y. General Features of Squall Lines in East China. *Mon. Weather Rev.* **2013**, *141*, 1629–1647. [[CrossRef](#)]
60. Xu, X.; Xue, M.; Wang, Y. Mesovortices within the 8 May 2009 Bow Echo over the Central United States: Analyses of the Characteristics and Evolution Based on Doppler Radar Observations and a High-Resolution Model Simulation. *Mon. Weather Rev.* **2015**, *143*, 2266–2290. [[CrossRef](#)]
61. Verlinde, J.; Cotton, W.R. Fitting Microphysical Observations of Nonsteady Convective Clouds to a Numerical Model: An Application of the Adjoint Technique of Data Assimilation to a Kinematic Model. *Mon. Wea. Rev.* **1993**, *121*, 2776–2793. [[CrossRef](#)]
62. Srivastava, R.C.; Coen, J.L. New Explicit Equations for the Accurate Calculation of the Growth and Evaporation of Hydrometeors by the Diffusion of Water Vapor. *J. Atmos. Sci.* **1992**, *49*, 1643–1651. [[CrossRef](#)]

Disclaimer/Publisher’s Note: The statements, opinions and data contained in all publications are solely those of the individual author(s) and contributor(s) and not of MDPI and/or the editor(s). MDPI and/or the editor(s) disclaim responsibility for any injury to people or property resulting from any ideas, methods, instructions or products referred to in the content.